ADVANCED ENERGY MATERIALS
www.advenergymat.de

MoS_2-Based All-Purpose Fibrous Electrode and Self-Powering Energy Fiber for Efficient Energy Harvesting and Storage

Jia Liang, Guoyin Zhu, Caixing Wang, Yanrong Wang, Hongfei Zhu, Yi Hu, Hongling Lv, Renpeng Chen, Lianbo Ma, Tao Chen, Zhong Jin, and Jie Liu**

Here an all-purpose fibrous electrode based on MoS_2 is demonstrated, which can be employed for versatile energy harvesting and storage applications. In this coaxial electrode, ultrathin MoS_2 nanofilms are grown on TiO_2 nanoparticles coated carbon fiber. The high electrochemical activity of MoS_2 and good conductivity of carbon fiber synergistically lead to the remarkable performances of this novel composite electrode in fibrous dye-sensitized solar cells (showing a record-breaking conversion efficiency of 9.5%) and high-capacity fibrous supercapacitors. Furthermore, a self-powering energy fiber is fabricated by combining a fibrous dye-sensitized solar cell and a fibrous supercapacitor into a single device, showing very fast charging capability (charging in 7 s under AM1.5G solar illumination) and an overall photochemical-electricity energy conversion efficiency as high as 1.8%. In addition, this wire-shaped electrode can also be used for fibrous Li-ion batteries and electrocatalytic hydrogen evolution reactions. These applications indicate that the MoS_2-based all-purpose fibrous electrode has great potential for the construction of high-performance flexible and wearable energy devices.

1. Introduction

The energy and environmental crisis has become a vital problem threatening human society. To design energy harvesting and storage devices with high-efficiency and eco-friendliness is of great importance.[1–3] In the past decades, lots of energy devices have been developed, such as dye-sensitized solar cells (DSSCs), supercapacitors, Li-ion batteries (LIBs), and fuel cells.[4–9] However, most of existing energy devices are with planar or bulky structures, which cannot fully meet the urgent demands of portable, flexible, and wearable applications. Therefore, the fabrication of fibrous energy devices has attracted enormous attentions recently.[10–21] However, so far the performances of fiber-shaped energy devices, such as DSSCs (Table S1, Supporting Information)[22–29] and supercapacitors (Table S2, Supporting Information)[30–41] are still lower than the corresponding planar devices, because it is difficult to find appropriate fibrous electrodes with high electrochemical activity and stability.

Fibrous carbon materials, including carbon nanotube fibers, graphene fibers, carbon fibers (CFs), as well as their hybrids, have been considered as a class of promising electrode materials for fibrous energy harvesting and storage devices, owing to their good conductivity, strong stiffness, high tensile strength, and light weight.[42–48] However, most of these carbon-based electrode materials are with intrinsically limited electrochemical activities, which significantly restrict their actual performances in fibrous energy devices. For instance, Zou and co-workers reported a fibrous DSSC constructed from bare CF-based counter electrode only showing a conversion efficiency of ≈1%.[47] By decorating $CoNi_2S_4$ nanoribbons on the CF electrode, the photovoltaic conversion efficiency was enhanced to ≈7%, but still lower than that of the planar DSSC.[47] In the aspect of supercapacitors, Lee and co-workers fabricated solid-state coaxial fibrous supercapacitors using all-carbon electrodes in polymer gel electrolyte, which retained only 46% of the initial capacitance as the scan rate was increased from 2 to 200 mV s^{-1}, indicating relatively low rate capability.[48] To further improve the performances of fibrous energy devices, a promising route is to develop appropriate composite fibrous electrodes based on carbon and other complementary active materials with high electrochemical activity and efficiency.

On the other hand, it is of great importance to integrate energy conversion and storage functions into a single device, which can remove unnecessary charging circuits and external electrical connections, and reduce the size and cost. It is noteworthy that the integrated energy devices with low weight and compact size are particularly suitable for portable and wearable electronic applications. For examples, it has been reported that

Dr. J. Liang, G. Zhu, C. Wang, Y. Wang, Dr. H. Zhu, Y. Hu, Dr. H. Lv, R. Chen, L. Ma, Dr. T. Chen, Prof. Z. Jin, Prof. J. Liu
Key Laboratory of Mesoscopic Chemistry of MOE and Collaborative Innovation Center of Chemistry for Life Sciences
School of Chemistry and Chemical Engineering
Nanjing University
Nanjing, Jiangsu 210093, China
E-mail: zhongjin@nju.edu.cn; j.liu@duke.edu
Prof. J. Liu
Department of Chemistry
Duke University
Durham, NC 27708, USA

DOI: 10.1002/aenm.201601208

planar solar cells can be stacked with supercapacitors or secondary batteries to simultaneously achieve photoelectric conversion and electrochemical energy storage (as shown in Table S3, Supporting Information).[49–56] Nevertheless, the integrated energy devices with conventional planar structure cannot fulfill the demands of flexibility and elasticity for portable devices. Recently, several attempts have been made to develop wire-shaped integrated energy devices by connecting a fibrous DSSC and a fibrous supercapacitor, termed as "power fiber", "energy wire" or "energy fiber" (see the bottom of Table S3, Supporting Information).[39,57–59] However, up to now the performances of energy fibers are still relatively low, because it is difficult to design a multifunctional electrode with high efficiencies for both energy harvesting and storage. Therefore, it is desirable to design an all-purpose electrode with excellent performances in versatile energy devices, and the self-powering energy fibers.

In this study, we demonstrate an all-purpose fibrous electrode based on MoS_2 that can be simultaneously employed in various energy harvesting and storage applications. This wire-shaped coaxial electrode was prepared by the growth of ultrathin MoS_2 nanofilms onto TiO_2 nanoparticle coated carbon fiber (CF@TiO_2@MoS_2). The high electrochemical activity of MoS_2 and good conductivity of CF synergistically lead to the remarkable performances in fibrous DSSCs and fibrous supercapacitors. Furthermore, a self-powering energy fiber with integrated functionalities of DSSC and supercapacitor is developed by using the CF@TiO_2@MoS_2 electrode as an essential component. As a result, this energy fiber exhibited very fast photocharging rate and a high overall photochemical-electricity energy conversion efficiency. Besides, the MoS_2 based electrode also shows good capability in fibrous LIBs and electrocatalytic hydrogen evolution reactions (HER).

2. Results and Discussion

The structure of coaxial fibrous CF@TiO_2@MoS_2 electrode is shown in **Figure 1**. For the preparation, a strand of commercially available CFs with high conductivity and flexibility (Figure S1, Supporting Information) was treated in $TiCl_4$ aqueous solution, and followed by hydrothermal treatment in a mixed solution containing Na_2MoO_4 and C_2H_5NS (as detailed in the Experimental Section of Supporting Information). In this way, a layer of TiO_2 nanoparticles were grown on CFs as a bifunctional film to provide nucleation sites for growing MoS_2 nanofilms and to enhance the performances of CFs by improving the surface area and catalytic activity. Following, ultrathin MoS_2 nanofilms were grown on TiO_2 nanoparticles coated CFs. The intention behind employing MoS_2 nanofilms as the active material can be ascribed to the following three reasons: (1) Due to the 2D structure, the MoS_2 nanofilms show ultrathin thickness and large surface area;[60,61] (2) Because there are many active sulfur sites on the surface and edges, the MoS_2 nanofilms reveal good catalytic activities;[60,61] (3) The MoS_2 nanofilms exhibit high energy storage capacity.[62,63] Based on these favorable features, the fibrous CF@TiO_2@MoS_2 electrode was found to be very efficient for various energy conversion and storage applications, including DSSCs, supercapacitors, LIBs, and HER, as illustrated in Figure 1. In addition, a self-powering energy fiber integrated by a fibrous DSSC and a fibrous supercapacitor was also fabricated by using a single CF@TiO_2@MoS_2 electrode, exhibiting high efficiencies of both solar-to-electricity conversion and electrochemical energy storage.

The structural features of pristine CF and CF@TiO_2 electrode were characterized by scanning electronic microscopy (SEM), as shown in Figure S2 of the Supporting Information. It should be noted that the decoration of TiO_2 nanoparticles on CF is very important for the further coating of MoS_2 nanofilms because it provides necessary nucleation sites for the growth of MoS_2. Without the treatment of $TiCl_4$ solution, very few MoS_2 nanofilms can be grown on CF, as shown in Figure S3 of the Supporting Information. We also found that the growth of MoS_2 nanofilms on CF@TiO_2 is much better than that on slightly oxidized CFs (Figure S4, Supporting Information). Moreover, the optimization of processing time in the $TiCl_4$ solution was explored, as shown in Figures S2 and S5a of the

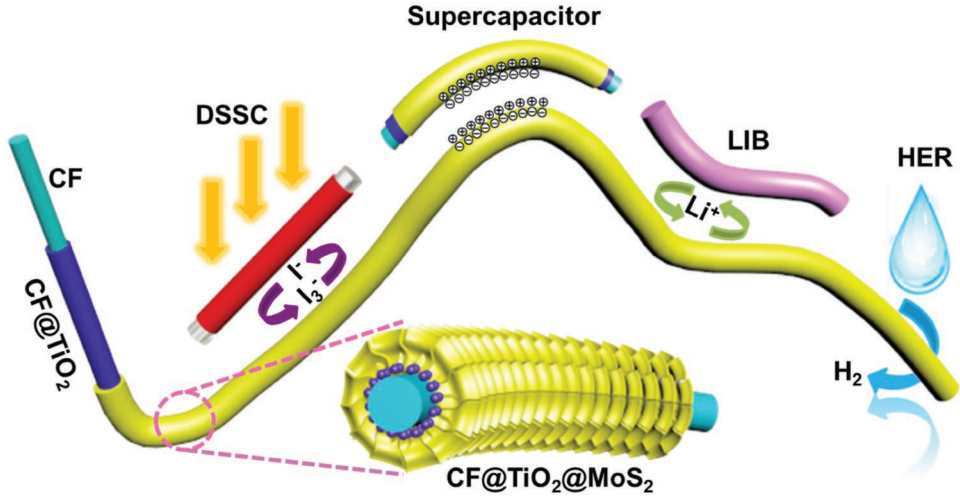

Figure 1. Schematic illustration of the structure of coaxial fibrous CF@TiO_2@MoS_2 electrode and its versatile applications for energy harvesting and storage, including fiber-shaped DSSCs, supercapacitors, LIBs, and flexible HER electrode.

Supporting Information. Similarly, the optimal synthesis condition of MoS_2 nanofilms in the mixed solution containing Na_2MoO_4 and C_2H_5NS was investigated as well, as shown in **Figure 2**a–c and Figure S5b of the Supporting Information. The SEM images of fibrous CF@TiO_2@MoS_2 electrodes obtained from the optimized synthesis condition at low and high magnifications (Figure 2a–c) revealed that the surface is uniformly covered by densely packed and wrinkled MoS_2 nanofilms. Figure 2d shows a SEM image and corresponding energy dispersive X-ray spectrometry (EDX) elemental mappings of the cross-section of a CF@TiO_2@MoS_2 electrode. The core of coaxial electrode is occupied by C element, while Ti, O, Mo, and S elements are evenly distributed in the outer shell, indicating that the CF is covered by the MoS_2 nanofilms with the help of TiO_2. Transmission electron microscopy (TEM) was also performed on as-prepared CF@TiO_2@MoS_2 electrode, which further revealed that the CF was fully covered by MoS_2 nanofilms (Figure 2e–g). Figure 2f shows most of the MoS_2 nanofilms are with very thin thickness. Clear lattice fringes can be observed in few-layered MoS_2 nanofilms (Figure 2g). The distance between two adjacent planes is ≈0.63 nm, which is in accordance with the interplanar spacing of (002) plane of hexagonal MoS_2 crystalline structure.[64,65]

X-ray photoelectron spectroscopy (XPS) analysis of CF@TiO_2@MoS_2 electrode was carried out (Figure S6, Supporting Information). The survey XPS spectrum (Figure S6a, Supporting Information) is consistent with the above result of EDX. Figure S6b–f of the Supporting Information present the high-resolution XPS spectra of C 1s, Ti 2p, O 1s, Mo 3d, and S 2p regions; the values of binding energies are listed in Table S4 of the Supporting Information. These data are in accordance with the characteristics of TiO_2 and MoS_2. The Raman spectra of CF@TiO_2@MoS_2 electrode are given in Figure S7 of the Supporting Information, which confirms the existence of carbon, TiO_2, and MoS_2.[66–68] Thermogravimetric analysis (TGA) was carried out on CF@TiO_2 and CF@TiO_2@MoS_2 electrodes, respectively, as shown in Figure S8 of the Supporting Information. The residue of CF@TiO_2 after TGA measurement is TiO_2 (≈0.7%). Owing to the oxidative reaction of MoS_2 to MoO_3 under air atmosphere, the residues of CF@TiO_2@MoS_2 after TGA measurement are TiO_2 and MoO_3. The weight percentage of the residues of CF@TiO_2@MoS_2 after TGA measurement is ≈6.9%. Therefore, the content of MoS_2 in CF@TiO_2@MoS_2 was calculated to be ≈6.89 wt%.

Fibrous DSSCs were constructed by using CF@TiO_2@MoS_2 to replace traditional platinum (Pt)-based counter electrode. **Figure 3**a shows a schematic diagram of a fibrous DSSC based on CF@TiO_2@MoS_2 counter electrode. The working electrode is a Ti wire covered with dye-sensitized TiO_2 nanotube array (Figure 3b). Figure S9a of the Supporting Information shows the TiO_2 nanotube array is vertically attached on the surface of the Ti wire and possesses a uniform alignment. Raman spectrum of the Ti microwire covered with TiO_2 nanotube array was also measured, as shown in Figure S9b of the Supporting Information, which is in accordance with the previous literature and consistent with anatase phase.[67] Figure 3c displays that the as-prepared fibrous DSSCs are very flexible to be bent into a circle or a heart-shape knot, and also can be winded around a glass rod. In principle, the overall power output of fibrous DSSCs is only limited by its length, which can be easily raised by increasing the length of the wire-shaped electrodes. Figure 3d shows a fibrous DSSC based on CF@TiO_2@MoS_2 with a length of 17 cm.

Cyclic voltammetry (CV) was employed to investigate the catalytic activity of as-produced electrodes toward tri-iodide

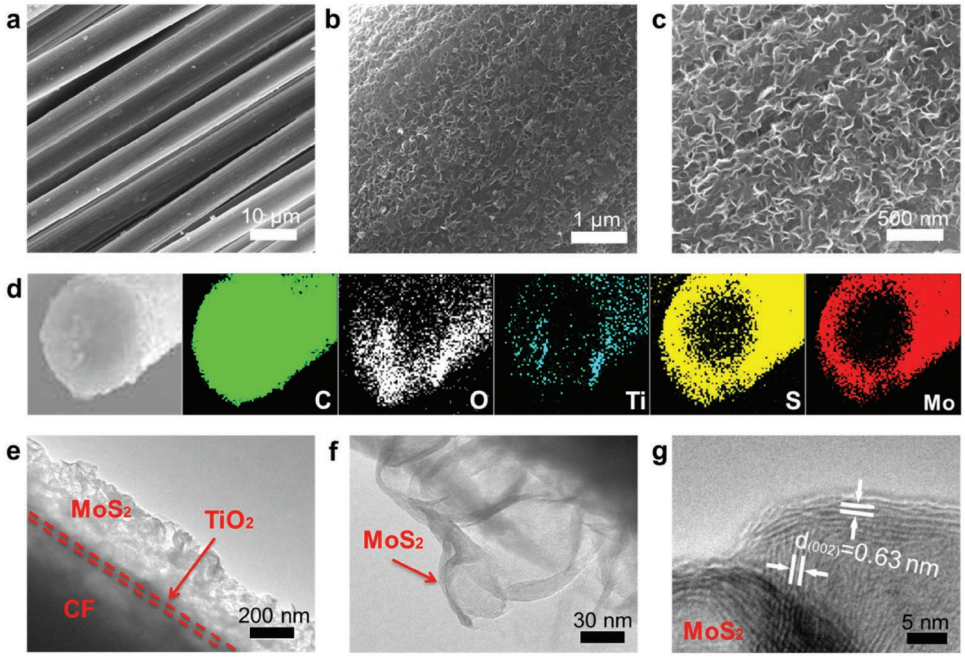

Figure 2. Structural characterizations of fibrous CF@TiO_2@MoS_2 electrode. a–c) SEM images of CF@TiO_2@MoS_2 electrode at different magnifications. d) SEM image and corresponding EDX elemental mapping of the cross-section of a CF@TiO_2@MoS_2 electrode. e–g) TEM images of CF@TiO_2@MoS_2 electrode. The lattice distance of 0.63 nm in (g) is assigned to the (002) planes of MoS_2.

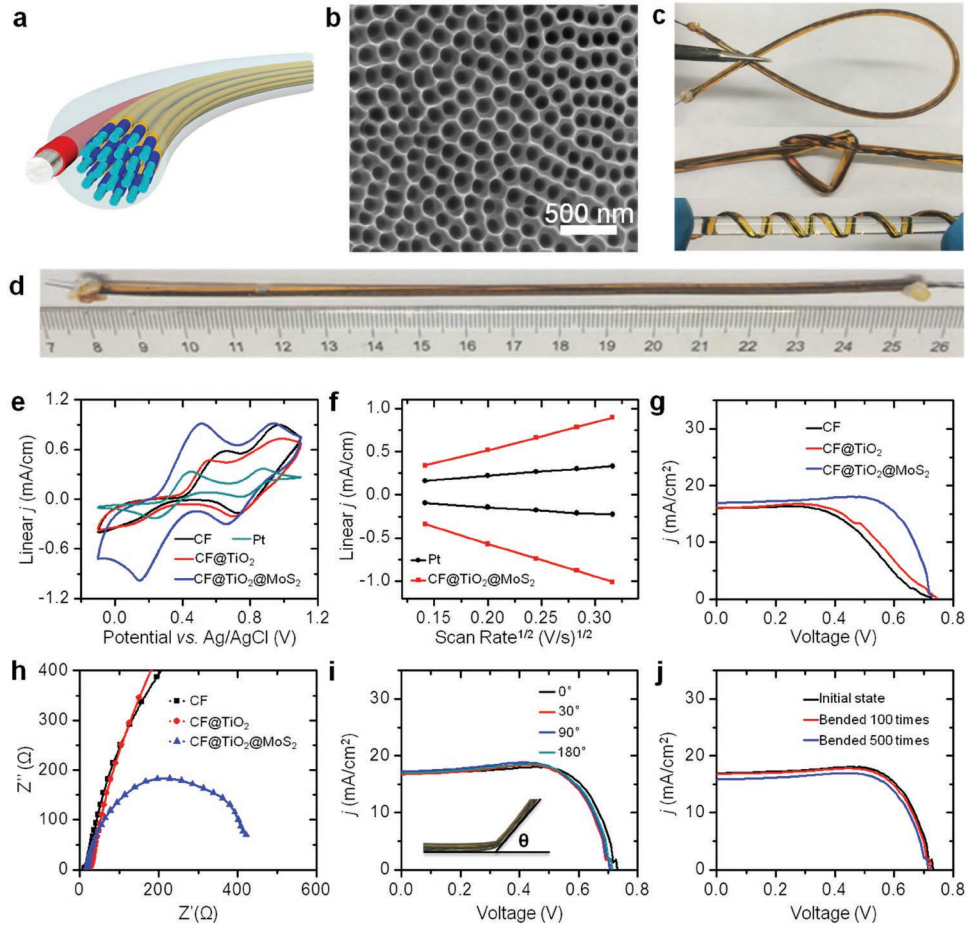

Figure 3. Fibrous DSSCs based on CF@TiO_2@MoS_2 electrode. a) Schematic illustration of a fibrous DSSC with CF@TiO_2@MoS_2 as counter electrode and dye-sensitized TiO_2 nanotube array coated Ti wire as working electrode. b) SEM image of TiO_2 nanotube array coated on the surface of Ti wire based working electrode. c) Optical images of fibrous DSSCs bended into various shapes. d) Optical image of a 17 cm long fibrous DSSC in the straight form. e) CV curves of pristine CF, CF@TiO_2, CF@TiO_2@MoS_2, and Pt counter electrodes at a scanning rate of 100 mV s^{-1} toward I^-/I_3^- redox couple, respectively. f) The peak current density of the left peak pairs as a function of the square root of the scan rates for Pt and CF@TiO_2@MoS_2 electrode. g) *J–V* plots and h) Nyquist plots of fibrous DSSCs based on pristine CF, CF@TiO_2, and CF@TiO_2@MoS_2 counter electrodes, respectively. i) *J–V* plots of fibrous DSSCs based on CF@TiO_2@MoS_2 counter electrode under different bending angles ($\theta = 0°$, 30°, 90°, and 180°, respectively). j) *J–V* plots of fibrous DSSCs based on CF@TiO_2@MoS_2 counter electrode at initial state and after different bending-unbending cycles at $\theta = 30°$.

reduction. Figure 3e shows the CV curves of the pristine CF, CF@TiO_2, CF@TiO_2@MoS_2, and Pt microwire counter electrodes toward I^-/I_3^- redox couple. Two pairs of redox peaks were shown in these CV curves. The left peak pair represents the redox transition between I_3^- and I^-, while the right peak pair represents I_2 and I_3^- transition. The electrocatalytic activity of the counter electrode material in the fibrous DSSC is directly related to the left oxidation–reduction peaks. Typically, the cathodic and anodic peaks on the left can be assigned to the reduction of I_3^- and the oxidation of I^-, respectively.[69] Clearly, the CF@TiO_2@MoS_2 electrode exhibits the highest electrocatalytic activity among the four samples. Moreover, the cycling stability of CF@TiO_2@MoS_2 based counter electrodes was measured by CV curves at a scanning rate of 100 mV s^{-1}, as shown in Figure S10 of the Supporting Information. The CV curve of CF@TiO_2@MoS_2 based counter electrode after 100 cycles almost completely overlaps with its initial CV curve. It indicates that the CF@TiO_2@MoS_2 based counter electrode has good stability during long-term tests. Figure S11 of the Supporting Information shows the CV curves of CF@TiO_2@MoS_2 and Pt microwire at various scan rates. Based on the data in Figure S11 of the Supporting Information, the anodic and cathodic peak current densities of the left peak pairs as a function of the square root of the scan rates were plotted (Figure 3f). The peak current density of fibrous CF@TiO_2@MoS_2 electrode is much larger than that of the Pt microwire, suggesting that CF@TiO_2@MoS_2 electrode is a promising candidate for replacing Pt microwire counter electrode in fibrous DSSCs.

The performances of as-prepared fibrous DSSCs were systematically studied. Figure 3g shows the *J–V* plots of fibrous DSSCs based on pristine CF, CF@TiO_2, and CF@TiO_2@MoS_2 counter electrodes, respectively. The corresponding photovoltaic parameters are listed in Table S1 of the Supporting Information. The CF@TiO_2@MoS_2 based fibrous DSSCs display an open-circuit voltage (V_{OC}) of 0.74 V, a short-circuit current density (J_{SC}) of 16.95 mA cm^{-2}, and a high fill factor (FF) of 0.75, resulting in a very high conversion efficiency (η) of 9.5%. In contrast, the fibrous DSSCs with pristine CF or CF@TiO_2

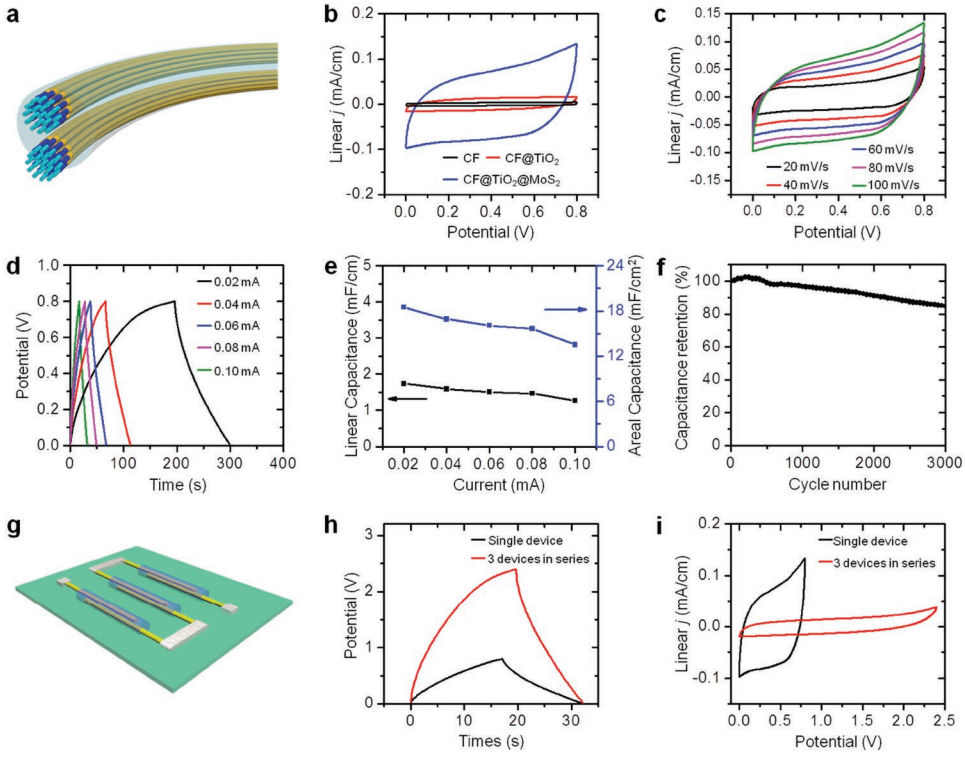

Figure 4. Fibrous supercapacitors based on CF@TiO_2@MoS_2 electrodes. a) Schematic illustration of a solid-state symmetric fibrous supercapacitor with CF@TiO_2@MoS_2 electrodes and PVA/H_3PO_4 gel electrolyte. b) CV curves of fibrous supercapacitors based on pristine CF, CF@TiO_2, and CF@TiO_2@MoS_2 electrodes at a scan rate of 100 mV s^{-1}, respectively. c) CV curves, d) galvanostatic charge/discharge curves, and e) linear and areal capacitances of CF@TiO_2@MoS_2 based fibrous supercapacitors, respectively. f) Performances of CF@TiO_2@MoS_2 based fibrous supercapacitors for 3000 cycles. g) Schematic diagram of an integrated high-voltage supercapacitor comprised of three in series-connected CF@TiO_2@MoS_2 based fibrous supercapacitors. h) Galvanostatic charge/discharge curves at a current of 0.10 mA and i) CV curves at a scan rate of 100 mV s^{-1} of the integrated high-voltage supercapacitor and an individual fibrous supercapacitor based on CF@TiO_2@MoS_2 electrodes, respectively.

counter electrodes only display V_{OC} of 0.74 or 0.75 V, J_{SC} of 16.05 or 16.10 mA cm^{-2}, FF of 0.51 or 0.54, η of 6.0% or 6.5%, respectively. It should be noted that, to the best of our knowledge, the η of 9.5% achieved by the CF@TiO_2@MoS_2 based fibrous DSSCs is the highest if comparing with other fibrous DSSCs in previous reports (Table S1, Supporting Information).[22–29] The dramatic increased FF and η of CF@TiO_2@MoS_2 based fibrous DSSCs is ascribed to the high electrocatalytic activity of MoS_2 and the rapid charge-transfer kinetic process occurring on the electrolyte-counter electrode interface. Figure 3h and Figure S12 of the Supporting Information show the Nyquist plots of the three kinds of fibrous DSSCs and the corresponding equivalent circuit, respectively, confirming the lowest charge transfer resistance (R_{ct}) of the CF@TiO_2@MoS_2 based fibrous DSSCs.

Moreover, we also tested the flexibility and stability of the fibrous DSSCs under bending deformation. Figure 3i shows the *J*–*V* plots of the CF@TiO_2@MoS_2 based fibrous DSSCs at different bending angles (θ). The corresponding photovoltaic parameters are listed in Table S5 of the Supporting Information. Figure 3i and Table S5 of the Supporting Information reveal that the η of the fibrous DSSC have no obvious change under different bending states. Furthermore, the *J*–*V* plots of CF@TiO_2@MoS_2 based fibrous DSSCs at initial state and after different bending–unbending cycles at $\theta = 30°$ were measured (Figure 3j), and the corresponding photovoltaic parameters are listed in Table S6 of the Supporting Information. After bending for 500 times, the η still can be maintained at 8.7% (≈92% retention of the initial state). The result indicates the excellent flexibility and robustness of CF@TiO_2@MoS_2 based fibrous DSSCs.

Fibrous CF@TiO_2@MoS_2 electrode is also applicable in wire-shaped supercapacitors. **Figure 4**a and Figure S13 of the Supporting Information show the schematic illustration and typical SEM image of solid-state symmetric fibrous supercapacitor based on CF@TiO_2@MoS_2 electrodes and polyvinyl alcohol (PVA)/H_3PO_4 gel electrolyte, respectively. As shown in Figure 4b, the CF@TiO_2@MoS_2 based fibrous supercapacitor displays the highest linear current density, suggesting it has superior energy storage capacity than pristine CF and CF@TiO_2 electrodes. The CV curves of CF@TiO_2@MoS_2 based fibrous supercapacitor at different scan rates were measured (Figure 4c). The shape of these CV curves is approximately rectangular, which indicates that CF@TiO_2@MoS_2 electrodes possess good electrochemical performances during charge/discharge processes. The galvanostatic charge/discharge curves of CF@TiO_2@MoS_2 based supercapacitors at different currents are nearly symmetric straight lines with similar shape (Figure 4d), indicating it is a typical double-layer supercapacitor which can be stably operated in a wide range of charging/discharging currents. The linear

capacitances (C_L) and areal capacitances (C_A) were calculated as well (Figure 4e). The values of C_L and C_A are 1740 μF cm^{-1} and 18.51 mF cm^{-2} at the current of 0.02 mA, which are remarkable when comparing to the previous results, as shown in Table S2 of the Supporting Information.[30–41] Notably, its capacitance retention was about 73% when the charging/discharging current increased from 0.02 to 0.10 mA, showing excellent rate capability. It is known that energy density and power density are two important parameters to evaluate the performances of supercapacitors. Figure S14 of the Supporting Information displays the Ragone plot of CF@TiO_2@MoS_2 based fibrous supercapacitor compared with previously reported fibrous supercapacitors.[33,35,36,44,70–72] The areal energy density of the device decreases from 1.65 to 1.21 μWh cm^{-2} as the power densities increases from 56.84 to 296.33 μW cm^{-2}, which are also remarkable when comparing to the previous results.[33,35,36,44,70–72] Moreover, the cyclic performance was examined by galvanostatic charge/discharge cycling at a current of 0.08 mA (Figure 4f). The fibrous supercapacitor still delivers ≈81% of its initial capacitance after 3000 cycles, confirming its good stability.

Electrochemical impedance spectroscopic (EIS) measurements were also performed on CF@TiO_2@MoS_2 based fibrous supercapacitors (Figure S15a, Supporting Information). The vertical line at low frequency and the low equivalent series resistance (≈100 Ω) indicate an ideal double-layer capacitive behavior. The flexibility and capacitance retention of CF@TiO_2@MoS_2 based fibrous supercapacitors at different bending angles was also measured (Figure S15b, Supporting Information), exhibiting a retention of 97% as the bending angle changes from 0° to 180°. This result implies the CF@TiO_2@MoS_2 based fibrous supercapacitors possess high stability toward bending. Figure 4g shows a schematic diagram of an integrated high-voltage supercapacitor consisted of three CF@TiO_2@MoS_2 based fibrous supercapacitors connected in series. In comparison with the 0.80 V operating voltage of an individual fibrous supercapacitor, the integrated high-voltage supercapacitor exhibits a broad voltage window of 2.40 V (Figure 4h,i).

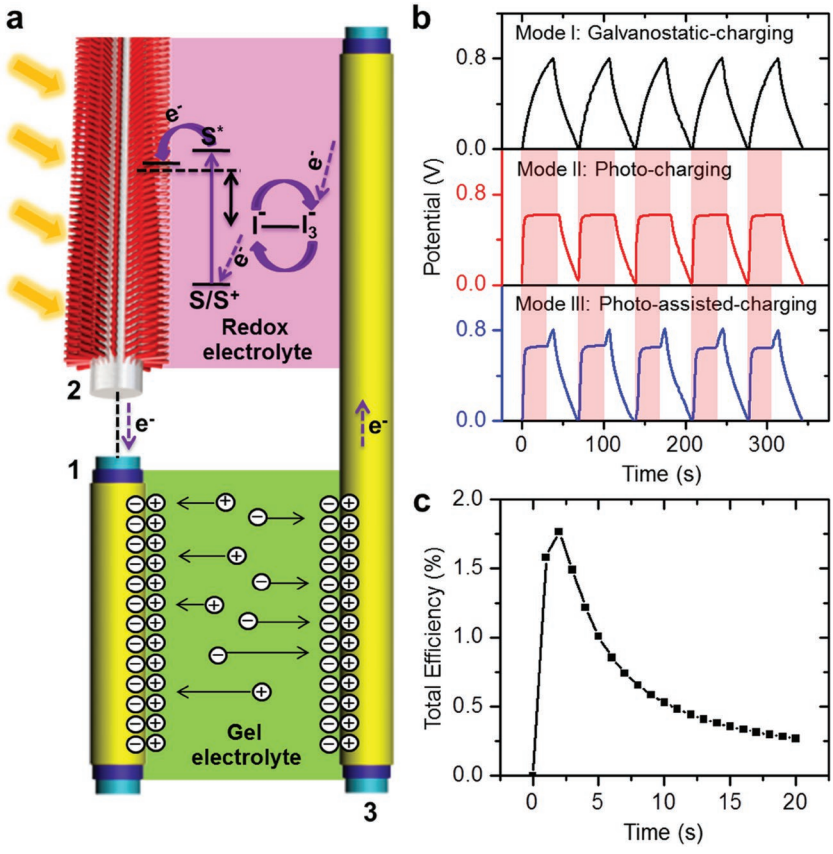

Figure 5. Performances of CF@TiO_2@MoS_2 based self-powering energy fiber. a) Schematic illustration and operational mechanism of a self-powering energy fiber constructed by integrating a fibrous DSSC and a fibrous supercapacitor with CF@TiO_2@MoS_2 electrodes. b) Galvanostatic-charging/galvanostatic-discharging (Mode I), photocharging/galvanostatic-discharging (Mode II) and photoassisted-charging/galvanostatic-discharging (Mode III) curves of the as-prepared self-powering energy fiber, respectively. The time periods of energy fiber under simulated AM1.5G (1 sun) light illumination are marked by light red areas. c) Overall photochemical-electricity energy conversion efficiency of the self-powering energy fiber as a function of the photocharging time.

In order to confirm that the CF@TiO_2@MoS_2 electrode can be simultaneously used for photoelectric conversion and electrochemical energy storage, an integrated self-powering energy fiber containing an energy harvesting part (fibrous DSSC) and an energy storage part (fibrous supercapacitor) has been fabricated, as illustrated in **Figure 5**a. In this energy fiber, a CF@TiO_2@MoS_2 electrode acts as both the counter electrode of DSSC part and the cathode of supercapacitor part. The working electrode of DSSC part is dye-sensitized TiO_2 nanotube array grown on Ti wire, while the anode of supercapacitor part is another CF@TiO_2@MoS_2 electrode. Figure 5a displays the charge transport route in the self-powering energy fiber during the photocharging stage. To achieve photocharging of the energy fiber under simulated AM1.5G solar irradiation (1 sun), the working electrode of DSSC part and the anode of supercapacitor part were connected during the charging stages. Upon illumination, dye molecules (N719) were shifted from ground state (S) to excited state (S*), and then the excited electrons were injected into the conduction band of TiO_2, leading to the oxidation of dye molecules (S*→S$^+$). At the following step, electrons were transported from the working electrode of DSSC to the anode of the supercapacitor. Meanwhile, the dye molecules returned to the ground state by receiving electrons generated from the oxidization of I^- ions to I_3^- ions. Then the I_3^- ions were diffused to the surface of CF@TiO_2@MoS_2 counter electrode and reduced to I^- ions by the catalysis of MoS_2 nanofilms. In this way, continuous light illumination on the DSSC part can achieve the transfer of electrons from the working electrode of the DSSC part to the anode of supercapacitor part, resulting in the fast charging of supercapacitor

part. When the voltage between cathode and anode is close to the V_{OC}, which is the potential between the conduction band of TiO_2 and the redox potential of the I^-/I_3^- electrolyte, the photocharging process will stop. Through this process, the self-powering energy fiber converts solar energy into electric energy by the DSSC part and then stores energy in the supercapacitor part. The stored electrochemical energy can be released by galvanostatic discharging, which is similar to that of conventional supercapacitors.

To investigate the charge/discharge behaviors of the self-powering energy fiber under different conditions, three kinds of testing modes, including galvanostatic-charging/galvanostatic-discharging (Mode I), photocharging/galvanostatic-discharging (Mode II), and photoassisted-charging/galvanostatic-discharging (Mode III) were employed, as detailed in the Experimental Section of Supporting Information. Figure 5b exhibits the corresponding charge/discharge curves of Modes I (black), Mode II (red), and Mode III (blue), respectively. At the galvanostatic charging stage of Mode I (without illumination), the supercapacitor needs ≈37 s to reach the cutoff voltage of 0.8 V by applying a constant charging current of 0.06 mA. While under the Mode II, the voltage of supercapacitor can approaches the V_{OC} (about 0.65–0.70 V) in just 7 s during the photocharging process under simulated solar illumination (marked by light red color), which is much faster than that under Mode I. Similarly, under Mode III, the supercapacitor only need ≈8 s to reach near the V_{OC} under illumination, which further demonstrates the photocharging is fast and effective as compared to the galvanostatic charging under a moderate charging current of 0.06 mA. Then, the voltage of supercapacitor can be raised to the cutoff voltage of 0.8 V by a subsequent galvanostatic charging step. It should be noted that, the voltage plateau during the photocharging process is slightly lower than the V_{OC}, which can be ascribed to the internal resistance of the self-powering energy fiber. Moreover, the conclusion that photocharging process is fast and effective compared to normal galvanostatic charging process is mainly summarized from the performance differences shown in Figure 3g, Figure 4e, and Figure 5b. The fast process of photocharging is mainly resulted from the high current obtained from the DSSCs. As shown in Figure 3g, the V_{OC}, J_{SC}, FF, and η of the CF@TiO_2@MoS_2 based fibrous DSSCs are 0.74 V, 16.95 mA cm^{-2}, 0.75, and 9.5%, respectively. Typically, the fibrous DSSC part of energy fiber has a length of 3 cm (with an effective area of ≈0.078 cm^2). Based on these data, the largest current generated by DSSCs can be estimated to be around 1.3 mA, which is much higher than that of normal charging/discharging current (0.02 to 0.10 mA, Figure 4d,e). Thus, the photocharging process is fast and effective as compared to normal galvanostatic charging process.

The overall photochemical-electricity energy conversion efficiency of as-prepared energy fiber was calculated using the following equation: $\eta = C*V^2/(2*P_{in}*S*t)$.[29–33] Here C and V are the capacitance and voltage of the energy storage part (fibrous supercapacitor), respectively; P_{in} is the energy density of incident light, S is the effective area of the energy harvesting part (fibrous DSSC), and t is the charging time. According to the photocharging/galvanostatic-discharging curve (Mode II) in Figure 5b, the overall photochemical-electricity energy conversion efficiency as a function of photocharging time is plotted in Figure 5c. As the photocharging time passes, the overall photochemical-electricity energy conversion efficiency first increases and then decreases (after 2.0 s), showing a maximum value of 1.8%, which is higher than the efficiency of other energy fibers in previous reports (Table S3, Supporting Information).[39,49–59]

In addition, we have found that CF@TiO_2@MoS_2 electrode can also be used in fibrous LIBs. Figure S16a of the Supporting Information shows the schematic diagram of a fibrous LIB consisted of a lithium metal wire anode and a fibrous CF@TiO_2@MoS_2 cathode. This fibrous LIB exhibits a high initial working voltage of 3.271 V (Figure S16b, Supporting Information) and can be used as a power source to light up a commercial red LED for about 5 min, as shown in Figure S16c of the Supporting Information. Figure S16d of the Supporting Information displays representative charge/discharge profiles of CF@TiO_2@MoS_2 based fibrous LIB measured between 0.01 and 3.0 V at a current rate of 3.0 mA m^{-1}. Specifically, in the first cycle, the fibrous LIB shows discharge and charge capacities of 71.3 and 40.1 mA h m^{-1}, respectively. The initial Coulombic efficiency is 56.2%, which can be ascribed to the formation of solid-electrolyte interface (SEI) films and the partial decomposition of the electrolyte.[73] The charge/discharge profiles of the subsequent cycles are different with the initial cycle (Figure S16d, Supporting Information). The discharge and charge capacities in the second cycle are 31.4 and 25.5 mA h m^{-1}, respectively, giving a higher Coulombic efficiency of 81.2%. Compared to those values of the second cycle, the discharge and charge capacities are retained as high as 76.1% (23.9 mA h m^{-1}) and 81.0% (20.6 mA h m^{-1}) after 20 charge–discharge cycles, with a Coulombic efficiency of 86.2%. These results suggest that in additional to fibrous DSSCs and supercapacitors, the CF@TiO_2@MoS_2 electrode also has the potential to be used in fibrous LIBs.

The HER catalytic activities were measured using the standard three-electrode electrochemical cell setup in 0.50 M H_2SO_4.[74–76] The pristine CF, CF@TiO_2 and CF@TiO_2@MoS_2 electrodes were employed as working electrode, respectively. The counter and reference electrodes were graphite rod and Ag/AgCl electrode, respectively. All of the experimental data have been *iR*-corrected by subtracting the Ohmic resistance loss from the overpotential. Figure S17a of the Supporting Information shows the Nyquist plots of the three working electrodes, which reveals the Ohmic resistances (R_s) of pristine CF, CF@TiO_2, and CF@TiO_2@MoS_2 electrodes are 9, 27, and 13 Ω, respectively. The pristine CF electrode displays the lowest R_s, while CF@TiO_2 shows the highest R_s, which can be ascribed to the high conductivity of CF and wide-bandgap of TiO_2. In Nyquist plots, the semicircle in high-frequency region is attributed to the charge transfer at the interface of working electrode/electrolyte, usually associating with R_{ct}. Because of the high conductivity, the R_{ct} of pristine CF electrode is almost zero. The CF@TiO_2@MoS_2 electrode reveals a lower R_{ct} value (3.1 Ω) than CF@TiO_2 (4.4 Ω), which can be attributed to the larger surface area and higher catalytic activity of CF@TiO_2@MoS_2. Figure S17b of the Supporting Information displays the polarization curves of the pristine CF, CF@TiO_2, and CF@TiO_2@MoS_2 electrodes, respectively, which were obtained at a voltage scanning rate of 5 mV s^{-1}. The CF@TiO_2@MoS_2 electrode exhibits much higher activity than the pristine CF and

$CF@TiO_2$ electrodes. This can be ascribed to the high catalytic activity and large surface area of MoS_2, comparable to the previous reports.[53,54] Specifically, the onset overpotentials of pristine CF, $CF@TiO_2$, and $CF@TiO_2@MoS_2$ electrodes are 454, 124, and 10 mV, respectively. Figure S17c of the Supporting Information shows the corresponding Tafel plots of the pristine CF, $CF@TiO_2$, and $CF@TiO_2@MoS_2$ electrodes, respectively. The linear portions of the Tafel slopes are fit to the Tafel equation ($(\eta = b\log(j) + a$, where b is the Tafel slope), yielding Tafel slopes of 130.8, 123.7, and 58.4 mV dec^{-1}, respectively. Clearly, the $CF@TiO_2@MoS_2$ electrode displays the smallest Tafel slope among the three working electrodes, indicating that the $CF@TiO_2@MoS_2$ electrode can prompt the largest catalytic current density at the same overpotential. This result shows the $CF@TiO_2@MoS_2$ electrode is a promising catalyst for HER. To evaluate the stability of $CF@TiO_2@MoS_2$ electrode during electrocatalytic hydrogen revolution in 0.50 M H_2SO_4, the polarization curves before and after 500 cycles CV sweeps are shown in Figure S17d of the Supporting Information. The polarization curve after 500 CV sweeps almost overlays with the initial curve, confirming that the $CF@TiO_2@MoS_2$ electrode possesses excellent stability in acidic solution.

3. Conclusion

In summary, an all-purpose fibrous $CF@TiO_2@MoS_2$ electrode was fabricated, and its performances in versatile energy harvesting and storage applications were tested. The fibrous DSSCs and supercapacitors constructed from this novel electrode exhibited superior performances than those in the literature. In addition, an integrated self-powering energy fiber was developed by combining a DSSC part and a supercapacitor part sharing a single fibrous $CF@TiO_2@MoS_2$ electrode. As a result, this energy fiber exhibited fast charging capability and remarkable energy efficiency. We also found that the $CF@TiO_2@MoS_2$ electrode can be used for fibrous LIBs and electrocatalytic HER. These applications, especially the integrated self-powering energy fiber, prove that the MoS_2-based fibrous electrode has great potential for the construction of novel and highly efficient power sources to support wearable and portable electronic devices.

Supporting Information

Supporting Information is available from the Wiley Online Library or from the author.

Acknowledgements

J.L. and G.Z. contributed equally to this work. This work was supported by the National Thousand Young Talents Program of China, the Young Scientists Project of National Basic Research Program of China (973 Program No. 2015CB659300), the National Natural Science Foundation of China (NSFC Grant Nos. 21403105 and 21573108), the China Postdoctoral Science Foundation (Grant Nos. 2015M580412, 2015M581768, and 2015M581774), the Natural Science Foundation for Young Scholars of Jiangsu Province (Grant Nos. BK20160647, BK20150571, and BK20150583), the Fundamental Research Funds for the Central Universities, and a project funded by the Priority Academic Program Development of Jiangsu Higher Education Institutions (PAPD).

Received: June 7, 2016
Revised: August 15, 2016
Published online:

[1] G. L. Che, B. B. Lakshmi, E. R. Fisher, C. R. Martin, *Nature* **1998**, *393*, 346.
[2] D. Yu, K. Goh, H. Wang, L. Wei, W. T. Jiang, Q. Zhang, L. M. Dai, Y. Chen, *Nat. Nanotechnol.* **2014**, *9*, 555.
[3] B. Oregan, M. Gratzel, *Nature* **1991**, *353*, 737.
[4] A. C. Dillon, K. M. Jones, T. A. Bekkedahl, C. H. Kiang, D. S. Bethune, M. J. Heben, *Nature* **1997**, *386*, 377.
[5] J. M. Tarascon, M. Armand, *Nature* **2001**, *414*, 359.
[6] I. Chung, B. Lee, J. He, R. P. H. Chang, M. G. Kanatzidis, *Nature* **2012**, *485*, 486.
[7] F. Dai, J. T. Zai, R. Yi, M. L. Gordin, H. Sohn, S. Chen, D. H. Wang, *Nat. Commun.* **2014**, *5*, 3605.
[8] F. Zheng, Y. Yang, Q. Chen, *Nat. Commun.* **2014**, *5*, 5261.
[9] Q. Liu, Z. F. Li, Y. D. Liu, H. Y. Zhang, Y. C. J. Ren, Sun, W. Q. Lu, Y. Zhou, L. Stanciu, E. A. Stach, J. Xie, *Nat. Commun.* **2015**, *6*, 6127.
[10] G. X. Qu, J. L. Cheng, X. D. Li, D. M. Yuan, P. N. Chen, X. L. Chen, B. Wang, H. S. Peng, *Adv. Mater.* **2016**, *28*, 3646.
[11] P. Chen, Y. F. Xu, S. S. He, X. M. Sun, S. W. Pan, J. Deng, D. Y. Chen, H. S. Peng, *Nat. Nanotechnol.* **2015**, *10*, 1077.
[12] Z. Yang, J. Ren, Z. T. Zhang, X. L. Chen, G. Z. Guan, L. B. Qiu, Y. Zhang, H. S. Peng, *Chem. Rev.* **2015**, *115*, 5159.
[13] Z. Zhang, K. P. Guo, Y. M. Li, X. Y. Li, G. Z. Guan, H. P. Li, Y. F. Luo, F. Y. Zhao, Q. Zhang, B. Wei, Q. B. Pei, H. S. Peng, *Nat. Photonics* **2015**, *9*, 233.
[14] J. Ren, Y. Zhang, W. Y. Bai, X. L. Chen, Z. T. Zhang, X. Fang, W. Weng, Y. G. Wang, H. S. Peng, *Angew. Chem. Int. Ed.* **2014**, *53*, 7864.
[15] H. Sun, X. You, Y. S. Jiang, G. Z. Guan, X. Fang, J. Deng, P. N. Chen, Y. F. Luo, H. S. Peng, *Angew. Chem. Int. Ed.* **2014**, *53*, 9526.
[16] Y. Fu, X. Cai, H. W. Wu, Z. B. Lv, S. C. Hou, M. Peng, X. Yu, D. C. Zou, *Adv. Mater.* **2012**, *24*, 5713.
[17] W. Wang, Q. Zhao, H. Li, H. W. Wu, D. C. Zou, D. P. Yu, *Adv. Funct. Mater.* **2012**, *22*, 2775.
[18] X. Chen, H. Lin, P. Chen, G. Guan, J. Deng, H. S. Peng, *Adv. Mater.* **2014**, *26*, 4444.
[19] W. X. Song, H. Wang, G. H. Liu, M. Peng, D. C. Zou, *Nano Energy* **2016**, *19*, 1.
[20] Y. W. Ma, P. Li, J. W. Sedloff, X. Zhang, H. B. Zhang, J. Liu, *ACS Nano* **2015**, *9*, 1352.
[21] Y. Xue, Y. Ding, J. Niu, Z. Xia, A. Roy, H. Chen, J. Ou, Z. Wang, L. Dai, *Sci. Adv.* **2015**, *1*, 1400198.
[22] J. Liang, G. Zhang, W. Sun, P. Dong, *Nano Energy* **2015**, *12*, 501.
[23] S. Pan, Z. B. Yang, H. P. Li, L. B. Qiu, H. Sun, H. S. Peng, *J. Am. Chem. Soc.* **2013**, *135*, 10622.
[24] G. Li, M. Peng, W. Song, H. Wang, D. Zou, *Nano Energy* **2015**, *11*, 341.
[25] T. Chen, L. M. Dai, *Angew. Chem. Int. Ed.* **2015**, *54*, 14947.
[26] X. Fang, Z. B. Yang, L. B. Qiu, H. Sun, S. W. Pan, J. Deng, Y. F. Luo, H. S. Peng, *Adv. Mater.* **2014**, *26*, 1694.
[27] S. Zhang, C. Y. Ji, Z. Q. Bian, P. R. Yu, L. H. Zhang, D. Y. Liu, E. Z. Shi, Y. Y. Shang, H. T. Peng, Q. Cheng, D. Wang, C. H. Huang, A. Y. Cao, *ACS Nano* **2012**, *6*, 7191.
[28] Z. B. Yang, J. Deng, X. M. Sun, H. P. Li, H. S. Peng, *Adv. Mater.* **2014**, *26*, 2643.

[29] J. Yan, M. J. Uddin, T. J. Dickens, D. E. Daramola, O. I. Okoli, *Adv. Mater. Interfaces* **2014**, *1*, 1400075.
[30] X. Chen, L. Qiu, J. Ren, G. Guan, H. Lin, Z. Zhang, P. Chen, Y. Wang, H. S. Peng, *Adv. Mater.* **2013**, *25*, 6436.
[31] Y. Li, K. Sheng, W. Yuan, G. Shi, *Chem. Commun.* **2013**, *49*, 291.
[32] H. Sun, X. You, J. Deng, X. Chen, Z. Yang, J. Ren, H. S. Peng, *Adv. Mater.* **2014**, *26*, 2868.
[33] G. Zhu, J. Chen, Z. Zhang, Q. Kang, X. Feng, Y. Li, Z. Huang, Y. Ma, *Chem. Commun.* **2016**, *52*, 2721.
[34] J. Ren, L. Li, C. Chen, X. Chen, Z. Cai, L. Qiu, Y. Wang, X. Zhu, H. S. Peng, *Adv. Mater.* **2013**, *25*, 1155.
[35] J. Ren, W. Bai, G. Guan, Y. Zhang, H. S. Peng, *Adv. Mater.* **2013**, *25*, 5965.
[36] Y. N. Meng, Y. Zhao, C. G. Hu, H. H. Cheng, Y. Hu, Z. P. Zhang, G. Q. Shi, L. T. Qu, *Adv. Mater.* **2013**, *25*, 2326.
[37] J. Wang, X. Li, Y. Zi, S. Wang, Z. Li, L. Zheng, F. Yi, S. Li, Z. L. Wang, *Adv. Mater.* **2015**, *27*, 4830.
[38] P. Xu, B. Wei, Z. Cao, J. Zheng, K. Gong, F. Li, J. Yu, Q. Li, W. Lu, J. H. Byun, B. S. Kim, Y. Yan, T. W. Chou, *ACS Nano* **2015**, *9*, 6088.
[39] T. Chen, L. Qiu, Z. Yang, Z. Cai, J. Ren, H. Li, H. Lin, X. Sun, H. S. Peng, *Angew. Chem. Int. Ed.* **2012**, *51*, 11977.
[40] P. Xu, T. Gu, Z. Cao, B. Wei, J. Yu, F. Li, J. H. Byun, W. Lu, Q. Li, T. W. Chou, *Adv. Energy Mater.* **2014**, *4*, 1300759.
[41] Z. Zhang, J. Deng, X. Li, Z. Yang, S. He, X. Chen, G. Guan, J. Ren, H. S. Peng, *Adv. Mater.* **2015**, *27*, 356.
[42] T. Chen, L. B. Qiu, Z. B. Cai, F. Gong, Z. B. Yang, Z. S. Wang, H. S. Peng, *Nano Lett.* **2012**, *12*, 2568.
[43] S. Zhang, C. Y. Ji, Z. Q. Bian, R. H. Liu, X. Y. Xia, D. Q. Yun, L. H. Zhang, C. H. Huang, A. Y. Cao, *Nano Lett.* **2011**, *11*, 3383.
[44] L. Kou, T. Q. Huang, B. N. Zheng, Y. Han, X. L. Zhao, K. Gopalsamy, H. Y. Sun, C. Gao, *Nat. Commun.* **2014**, *5*, 3754.
[45] L. B. Liu, Y. Yu, C. Yan, K. Li, Z. J. Zheng, *Nat. Commun.* **2015**, *6*, 7260.
[46] X. Yu, X. Su, K. Yan, H. Hu, M. Peng, X. Cai, D. C. Zou, *Adv. Mater. Technol.* **2016**, *1*, 2365.
[47] L. Chen, Y. Zhou, H. Dai, T. Yu, J. G. Liu, Z. G. Zou, *Nano Energy* **2015**, *11*, 697.
[48] V. T. Le, H. Kim, A. Ghosh, J. Kim, J. Chang, Q. A. Vu, D. T. Pham, J. H. Lee, S. W. Kim, Y. H. Lee, *ACS Nano* **2013**, *7*, 5940.
[49] J. Xu, H. Wu, L. F. Lu, S. F. Leung, D. Chen, X. Y. Chen, Z. Y. Fan, G. Z. Shen, D. D. Li, *Adv. Funct. Mater.* **2014**, *24*, 1840.
[50] P. Liu, H. X. Yang, X. P. Ai, G. R. Li, X. P. Gao, *Electrochem. Commun.* **2012**, *16*, 69.
[51] Z. B. Yang, L. Li, Y. F. Luo, R. X. He, L. B. Qiu, H. J. Lin, H. S. Peng, *J. Mater. Chem. A* **2013**, *1*, 954.
[52] C. Y. Hsu, H. W. Chen, K. M. Lee, C. W. Hu, K. C. Ho, *J. Power Sources* **2012**, *195*, 6232.
[53] A. P. Cohn, W. R. Erwin, K. Share, L. Oakes, A. S. Westover, R. E. Carter, R. Bardhan, C. L. Pint, *Nano Lett.* **2015**, *15*, 2727.
[54] N. F. Yan, G. R. Li, G. L. Pan, X. P. Gao, *J. Electrochem. Soc.* **2012**, *159*, A1770.
[55] P. Liu, Y. L. Cao, G. R. Li, X. P. Gao, X. P. Ai, H. X. Yang, *ChemSusChem* **2013**, *6*, 802.
[56] M. Z. Yu, W. D. McCulloch, D. R. Beauchamp, Z. J. Huang, X. D. Ren, Y. Y. Wu, *J. Am. Chem. Soc.* **2015**, *137*, 8332.
[57] Y. P. Fu, H. W. Wu, S. Y. Ye, X. Cai, X. Yu, S. C. Hou, H. Kafafy, D. C. Zou, *Energy Environ Sci.* **2013**, *6*, 805.
[58] Z. B Yang, J. Deng, H. Sun, J. Ren, S. W. Pan, H. S. Peng, *Adv. Mater.* **2014**, *26*, 7038.
[59] X. L. Chen, H. Sun, Z. B. Yang, G. Z. Guan, Z. T. Zhang, L. B. Qiu, H. S. Peng, *J. Mater. Chem. A* **2014**, *2*, 1897.
[60] M. Acerce, D. Voiry, M. Chhowalla, *Nat. Nanotechnol.* **2015**, *10*, 313.
[61] H. I. Karunadasa, E. Montalvo, Y. J. Sun, M. Majda, J. R. Long, C. J. Chang, *Science* **2012**, *335*, 698.
[62] X. Li, J. Y. Zhang, R. Wang, H. Y. Huang, C. Xie, Z. H. Li, J. Li, C. M. Niu, *Nano Lett.* **2015**, *15*, 5268.
[63] T. Stephenson, Z. Li, B. Olsen, D. Mitlin, *Energy Environ. Sci.* **2014**, *7*, 209.
[64] S. Najmaei, Z. Liu, W. Zhou, X. L. Zou, G. Shi, S. D. Lei, B. I. Yakobson, J. C. Idrobo, P. M. Ajayan, J. Lou, *Nat. Mater.* **2013**, *12*, 754.
[65] J. Xie, J. J. Zhang, S. Li, F. Grote, X. D. Zhang, H. Zhang, R. X. Wang, Y. Lei, B. C. Pan, Y. Xie, *J. Am. Chem. Soc.* **2013**, *135*, 17881.
[66] A. C. Ferrari, J. C. Meyer, V. Scardaci, C. Casiraghi, M. Lazzeri, F. Mauri, S. Piscanec, D. Jiang, K. S. Novoselov, S. Roth, A. K. Geim, *Phys. Rev. Lett.* **2006**, *97*, 187401.
[67] T. Ohsaka, F. Izumi, Y. Fujiki, *J. Raman. Spectrosc.* **1978**, *6*, 321.
[68] H. Li, Q. Zhang, C. C. R. Yap, B. K. Tay, T. H. T. Edwin, A. Olivier, D. Baillargeat, *Adv. Funct. Mater.* **2012**, *7*, 1385.
[69] J. Zhang, S. Najmaei, H. Lin, J. Lou, *Nanoscale* **2014**, *6*, 5279.
[70] J. Bae, M. K. Song, Y. J. Park, J. M. Kim, M. L. Liu, Z. L. Wang, *Angew. Chem. Int. Ed.* **2011**, *50*, 1683.
[71] F. Su, X. Lv, M. Miao, *Small* **2015**, *11*, 854.
[72] H. Xu, X. Hu, Y. Sun, H. Yang, X. Liu, Y. Huang, *Nano Res.* **2015**, *8*, 1148.
[73] G. Huang, F. F. Zhang, X. C. Du, J. W. Wang, D. M. Yin, L. M. Wang, *Chem. Eur. J.* **2014**, *35*, 11214.
[74] D. J. Li, U. N. Maiti, J. Lim, D. S. Choi, W. J. Lee, Y. Oh, G. Y. Lee, S. O. Kim, *Nano Lett.* **2014**, *14*, 1228.
[75] C. Tsai, F. Abild-Pedersen, J. K. Norskov, *Nano Lett.* **2014**, *14*, 1381.
[76] J. Lin, Z. W. Peng, G. Wang, D. Zakhidov, E. Larios, M. J. Yacaman, J. M Tour, *Adv. Energy Mater.* **2014**, *4*, 1301875.